PROCEEDINGS OF SCIENCE

Search for Heavy Neutrino in $K^- \to \mu^- \nu_h(\nu_h \to \nu\gamma)$ Decay at ISTRA+ Setup

V. A. Duk[*†]
Institute for Nuclear Research of RAS, Moscow, Russia
E-mail: Viacheslav.Duk@cern.ch

Heavy neutrino ν_h with $m_h \lesssim 300MeV$ can be effectively searched for in kaon decays. We put upper limits on mixing matrix element $|U_{\mu h}|^2$ for radiatively decaying ν_h from $K^- \to \mu^- \nu_h(\nu_h \to \nu\gamma)$ decay chain in the following parameter region: $40MeV \leq m_h \leq 80MeV; 10^{-11}sec \leq \tau_h \leq 10^{-9}sec$. For all masses $|U_{\mu h}|^2 \lesssim 7 \cdot 10^{-5}$ for Majorana type of ν_h and $|U_{\mu h}|^2 \lesssim 3 \cdot 10^{-5}$ for the Dirac case.

The XXth International Workshop High Energy Physics and Quantum Field Theory
September 24-October 1, 2011
Sochi Russia

[*]Speaker.
[†]for the ISTRA+ collaboration.

PoS(QFTHEP2011)013

1. Introduction

For more than ten years latest results of short-baseline neutrino experiments have been widely discussed and still there is no clear understanding of an event excess observed by LSND [1] and MiniBooNE [2, 3] experiments and their contradiction with KARMEN [4] results.

Oscillation interpretations of the event excess require additional sterile neutrino(s) with $\Delta m \sim 1eV^2$ (see [5] for review). An alternative interpretation of the results of all three experiments is proposed in [6]. Below we briefly discuss results obtained in that paper.

The main idea (proposed for the first time in [7]) is that in the experiments mentioned above signals from electrons and photons are indistinguishable. One could introduce heavy sterile neutrino ν_h as a component of ν_μ flavor eigenstate with a corresponding mixing matrix element $U_{\mu h}$ which is produced in ν_μ neutral current (NC) interactions and decays radiatively into a photon and a light neutrino ν. The decay channel $\nu_h \to \nu\gamma$ is dominant if there is a large enough magnetic transition moment μ_{tr} (it requires substantial new physics because in a minimally extended SM μ_{tr} is not large enough, see [8]). In this case event excess in LSND and MiniBooNE experiments comes from photons and not from electrons. In KARMEN experiment, ν_h's with $m > 40MeV$ cannot be produced within the detector because of a kinematic threshold effect.

Sterile neutrino ν_h could be either of Dirac or Majorana type. In the latter case a photon angular distribution in ν_h rest frame is isotropic while for the Dirac case there is an anisotropy depending on ν_h mass: $\frac{dN}{dcos\theta^\star} \sim (1 + \frac{m_\mu^2 - m_h^2}{m_\mu^2 + m_h^2} cos\theta^\star)$.

Combined analysis of LSND, KARMEN and MiniBooNE data results in the following properties of ν_h (regardless of the neutrino type):

- $40MeV \lesssim m_h \lesssim 80MeV$;
- $10^{-11}sec \lesssim \tau_h \lesssim 10^{-9}sec$;
- $10^{-3} \lesssim |U_{\mu h}|^2 \lesssim 10^{-2}$.

It was mentioned that ν_h could be considered as a component of ν_μ. This leads to a very important consequence that ν_h is also produced in charged current (CC) interactions and can be effectively searched for in pion and kaon decays (this idea was proposed in [9]).

The simplest way to do it is to study two-body decays $\pi \to \mu\nu$ and $K \to \mu\nu$ and look for a peak in a muon energy distribution ($E_\mu = (M^2 + m_\mu^2 - m_h^2)/2M$) below the main one from $\pi \to \mu\nu_\mu$ ($\pi_{\mu 2}$) and $K \to \mu\nu_\mu$ ($K_{\mu 2}$). These decays allow to search for ν_h with masses up to ~300 MeV.

Experimental limits from $\pi_{\mu 2}$ decay [10] were obtained for $5MeV \leq m_h \leq 30MeV$: $|U_{\mu h}|^2 < 10^{-5} - 10^{-3}$. Best limits for kaon decays come from KEK experiment [11]: $|U_{\mu h}|^2 < 10^{-4}$ for $70MeV \leq m_h \leq 300MeV$. $\pi_{\mu 2}$ decay is not sensitive to large m_h masses, while $K_{\mu 2}$ decay is not sensitive to low m_h masses because of resolution effects and strong background from $K \to \mu\nu_\mu\gamma(K_{\mu 2\gamma})$ decay. Thus, a region $30MeV < m_h < 70MeV$ is not constrained at all. One should notice that limits above were obtained for relatively long-lived neutrinos flying away from a detector (photon veto was applied in both cases).

Another possibility to search for heavy neutrino in kaon decays (which we are going to use) is to measure $K \to \mu\nu_h(\nu_h \to \nu\gamma)$ decay chain. In this case the background from $K_{\mu 2}$ is small and

one can search for ν_h in a low mass region (background from $K_{\mu 2\gamma}$ is also small, see Section 4). One should stress here that only the case of radiatively decayed neutrinos is considered.

The main purpose of this paper is to search for heavy neutrino in $K^- \to \mu^- \nu_h(\nu_h \to \nu\gamma)$ with properties described in [6] and in the following parameter range: $40MeV \leq m_h \leq 80MeV$, $10^{-11}sec \leq \tau_h \leq 10^{-9}sec$.

2. ISTRA+ setup

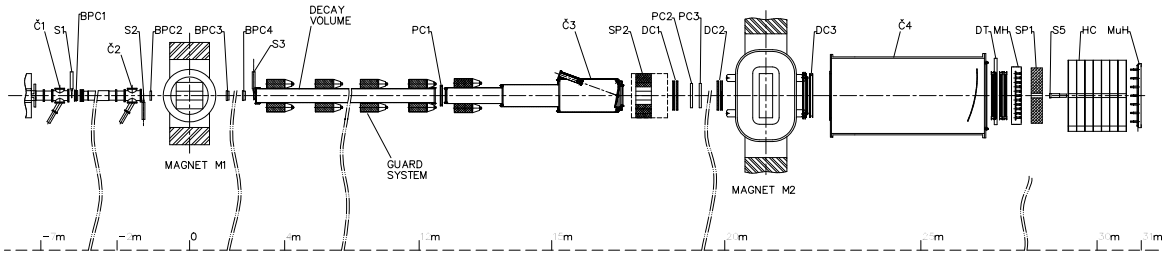

Figure 1: Elevation view of the ISTRA+ detector.

The experiment was performed at the IHEP 70 GeV proton synchrotron U-70. The experimental setup ISTRA+ (Fig. 1) was described in details in [12]. The setup was located in the negative unseparated secondary beam. The beam momentum in the measurements was ~ 26 GeV with $\Delta p/p \sim 1.5\%$. The fraction of K^- in the beam was $\sim 3\%$. The beam intensity was $\sim 3 \cdot 10^6$ per 1.9 sec U-70 spill. The track of a beam particle deflected by M_1 was measured by $BPC_1 - BPC_4$ (1mm step multiwire chambers), the kaon identification was done by $\check{C}_0 - \check{C}_2$ threshold Cherenkov counters. A 9 meter long vacuum decay volume was surrounded by Guard System (GS) – 8 lead glass rings $LG_1 - LG_8$ used to veto low energy photons. SP_2 was a lead glass calorimeter to detect/veto large angle photons. Tracks of decay products deflected in M_2 with 1Tm field integral were measured by $PC_1 - PC_3$ (2mm step proportional chambers); $DC_1 - DC_3$ (1cm cell drift chambers) and finally by 2cm diameter drift tubes $DT_1 - DT_4$. Wide aperture threshold Cherenkov counters $\check{C}_3$, $\check{C}_4$ were filled with He and were not used in the measurements. Nevertheless $\check{C}_3$ was used as an extension of the decay volume. SP_1 ($ECAL$) was a 576-cell lead glass calorimeter, followed by HC ($HCAL$) – a scintillator-iron sampling hadron calorimeter. HC was subdivided into 7 longitudinal sections 7×7 cells each. MH was a 11×11 cell scintillating hodoscope used to improve the time resolution of the tracking system, MuH was a 7×7 cell muon hodoscope.

The trigger was provided by $S_1 - S_3$, S_5 scintillation counters, $\check{C}_0 - \check{C}_2$ Cherenkov counters, analog sum of amplitudes from the last dinodes of the SP_1 : $T_0 = S_1 \cdot S_2 \cdot S_3 \cdot \check{C}_0 \cdot \bar{\check{C}}_1 \cdot \bar{\check{C}}_2 \cdot \bar{S}_5 \cdot \Sigma(SP_1)$, here S_5 was a counter downstream the setup at the beam focus; $\Sigma(SP_1)$ – a requirement for the analog sum of $ECAL$ amplitudes to be above $\sim$3 GeV. The last requirement served to suppress the $K_{\mu 2}$ decay.

3. Event reconstruction

Event reconstruction for $K^- \to \mu^- \nu_h(\nu_h \to \nu\gamma)$ is nearly the same as for $K^- \to \mu^- \nu_\mu \gamma$. The only difference is that for $K^- \to \mu^- \nu_\mu \gamma$ it is possible to reconstruct gamma momentum in a laboratory frame $\vec{p}_\gamma^{\,lab}$ using the decay vertex and a shower centre while for $K^- \to \mu^- \nu_h(\nu_h \to \nu\gamma)$ the photon is emitted from a secondary vertex which is unknown. Nevertheless one can reconstruct $\vec{p}_\gamma^{\,lab}$ using a primary vertex. This leads to an additional photon energy smearing in a kaon rest frame.

In Fig. 2 the normalized difference between the measured and true photon energy in the kaon rest frame is shown. For $\tau_h = 10^{-11} sec$ this difference is dominated by resolution effects while for large τ one can see additional smearing. Typical values of photon transverse momentum with respect to ν_h momentum are small, that is why smearing is not crucial.

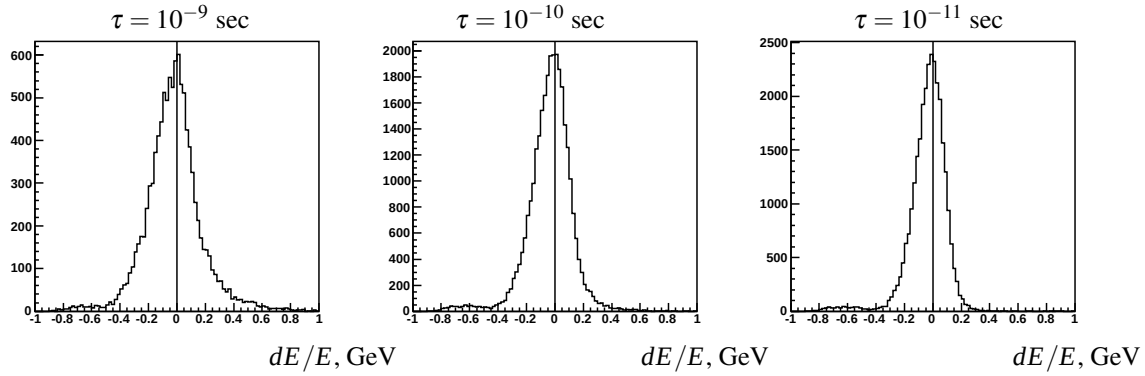

Figure 2: Photon energy smearing in the kaon rest frame: $dE/E = (E_{measured} - E_{true})/E_{true}$ (MC data, $m = 60 MeV$).

4. Event selection

The decay signature is defined as follows: one primary track (kaon); one negatively charged secondary track identified as muon; one shower in *ECAL* not associated with the charged track. Muon identification using *ECAL* and *HCAL* is described in our previous papers ([14, 15]).

The event selection for $K^- \to \mu^- \nu_h(\nu_h \to \nu\gamma)$ is very similar to that of $K^- \to \mu^- \nu_\mu \gamma$. Standard kinematic variables are used for the further analysis: $x = 2E_\gamma/m_K$ and $y = 2E_\mu/m_K$, E_γ and E_μ being photon and muon energies in the kaon rest frame. As in [13], Dalitz-plot will be used for studying signal and background kinematic regions.

The main background comes from 3 decay modes: $K^- \to \mu^- \bar{\nu}_\mu \gamma(K_{\mu 2\gamma})$, $K^- \to \mu^- \bar{\nu}_\mu \pi^0(K_{\mu 3})$ with one gamma lost from $\pi^0 \to \gamma\gamma$ and $K^- \to \pi^- \pi^0(K_{\pi 2})$ with one gamma lost and π misidentified as μ. Dalitz-plot distributions for the signal, $K_{\mu 2\gamma}$, $K_{\mu 3}$ and $K_{\pi 2}$ are shown in Figs. 3 – 6.

4.1 Signal signatures for $K \to \mu \nu_h(\nu_h \to \nu\gamma)$

The simplest way to observe heavy neutrino is to look for a peak in E_μ – muon energy in the kaon rest frame (see Section 1). Another signature comes from a photon angular distribution in the

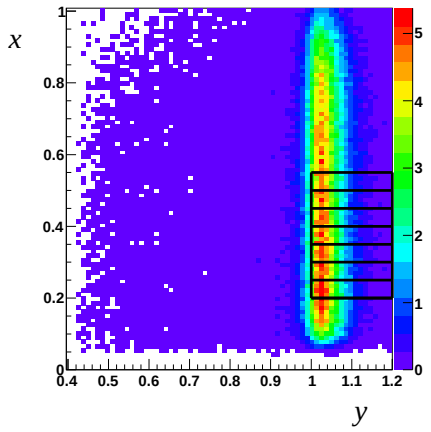

Figure 3: Dalitz-plot density for the signal ($m = 60MeV$, $\tau = 10^{-10}sec$).

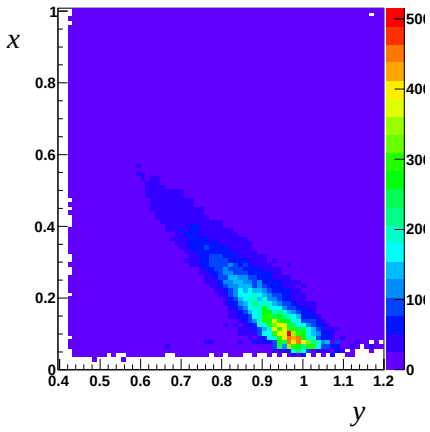

Figure 4: Dalitz-plot density for the $K_{\mu 2\gamma}(IB)$ background.

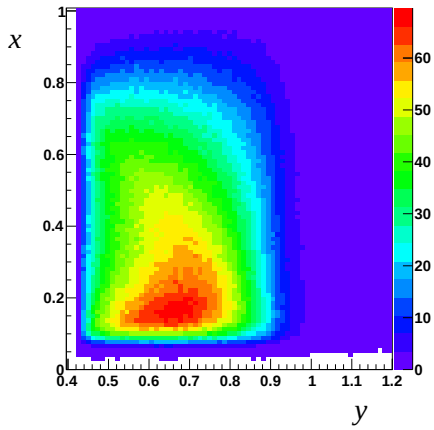

Figure 5: Dalitz-plot density for the $K_{\mu 3}$ background.

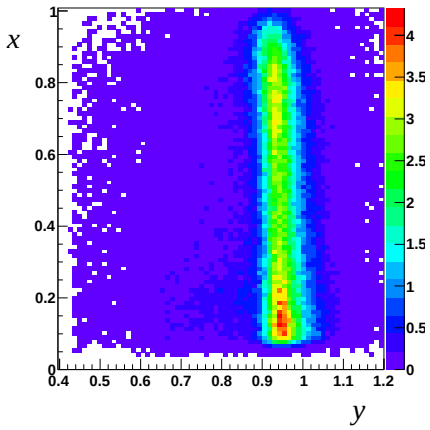

Figure 6: Dalitz-plot density for the $K_{\pi 2}$ background.

kaon rest frame. Distributions over $cos\theta_{\mu\gamma}$ and y for Dirac and Majorana cases are shown in Fig. 7. It can be seen that the difference in y and $cos\theta_{\mu\gamma}$ shapes is negligible for two neutrino types.

4.2 Signal extraction procedure

The procedure starts with dividing all kinematic (y,x) region into stripes on x (x-stripes). The x-stripe width is Δx=0.05 ($\Delta E_\gamma \sim 12MeV$). In every x-stripe we put a cut on y: $1.0 < y < 1.2$ to suppress backgrounds.

For each x-stripe we do simultaneous fit of two histograms – $cos\theta_{\mu\gamma}$ (with the cut on y introduced above) and y (without this cut).

4.3 Selected kinematic region

For further analysis we have selected seven x-stripes in the following region: $0.2 < x <$

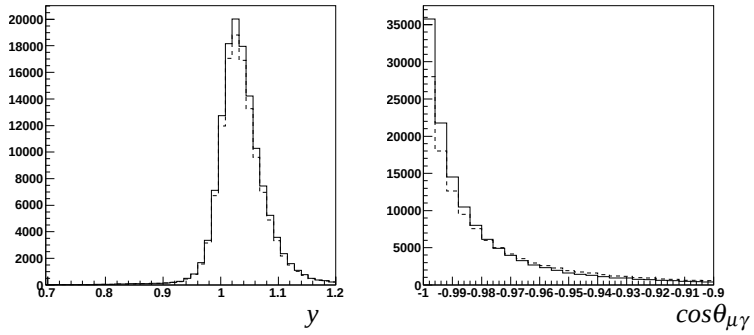

Figure 7: Dirac (solid) and Majorana (dash) type of ν_h ($m = 60MeV$, $\tau = 10^{-10}sec$). Left: distribution over normalized muon energy $y = 2E_\mu/m_K$. Right: $cos\theta_{\mu\gamma}$ in the kaon rest frame.

0.55 $(49MeV < E_\gamma < 136MeV)$. Selected x-stripes are shown in Fig. 3. Experimental Dalitz-plot with selected x-stripes is shown in Fig. 8.

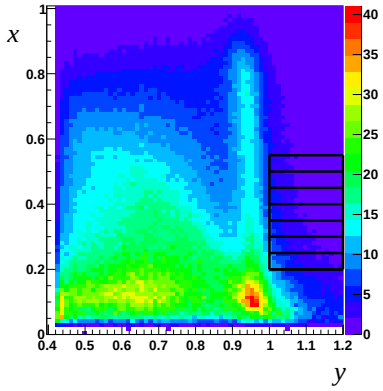

Figure 8: Dalitz-plot density for the data.

4.4 Simultaneous fit results

As an example, the results of simultaneous fits in x-stripes 3 and 5 are shown in Fig. 9, 10. Both signal and background shapes are taken from MC.

The simultaneous fit gives signal event number in each x-stripe. As we use the same data several times we should take care about the correct estimation of a statistical error. The whole procedure of the simultaneous fit is as follows:

- do simultaneous fit of two histograms and obtain $\{p_i\}$ – best parameter values (they correspond to global χ^2 minimum);
- take $\{p_i\}$ as initial values and perform χ^2/ndf and error estimation for one histogram cos $\theta_{\mu\gamma}$ using a single call of MINOS program [16].

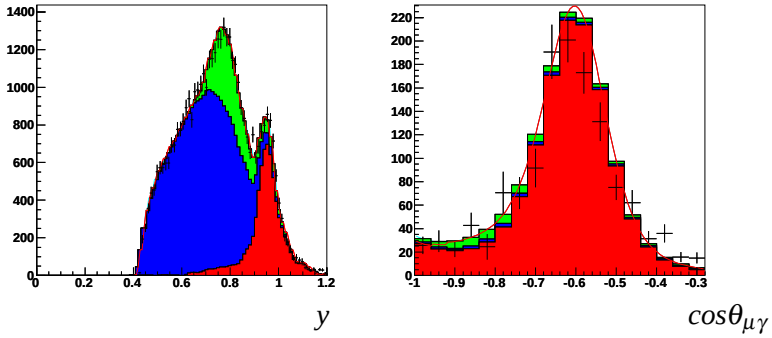

Figure 9: Simultaneous fit for $m = 60MeV$, $\tau = 10^{-10}sec$. Stripe 3 ($0.3 < x < 0.35$). $\chi^2/n.d.f. = 162.6/81$. Points with errors – data, magenta – signal, red – $K_{\pi 2}$, blue – $K_{\mu 3}$, green – $K_{\mu 2\gamma}$.

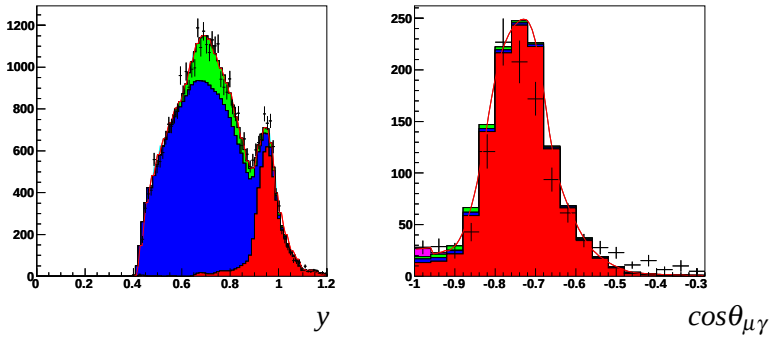

Figure 10: Simultaneous fit for $m = 60MeV$, $\tau = 10^{-10}sec$. Stripe 5 ($0.4 < x < 0.45$). $\chi^2/n.d.f. = 188.3/81$. Points with errors – data, magenta – signal, red – $K_{\pi 2}$, blue – $K_{\mu 3}$, green – $K_{\mu 2\gamma}$.

5. Upper limit on $|U_{\mu h}|^2$

5.1 $|U_{\mu h}|^2$ extraction from x-stripes

From the simultaneous fit we get $N_{exp}(K \to \mu\nu_h)$ for each x-stripe. This event number should be transformed into $|U_{\mu h}|^2$. This could be done either for each x-stripe or for all selected kinematic region. To avoid systematics depending on an x-stripe (for example backgrounds could be described worse by MC in a certain x-stripe and shift a total result) we use the first method.

As a normalization it is natural to use $K_{\mu 2\gamma}$ decay. The main formula is the following:

$$\frac{N_{exp}(K \to \mu\nu_h)}{N_{exp}(K_{\mu 2\gamma})} = \frac{BR(K \to \mu\nu_h)}{BR(K_{\mu 2\gamma})} \frac{\varepsilon(K \to \mu\nu_h)}{\varepsilon(K_{\mu 2\gamma})}.$$

$N_{exp}(K_{\mu 2\gamma})$ is taken from our previous analysis [13] in a wide kinematic region, $\varepsilon(K \to \mu\nu_h)$ and $\varepsilon(K_{\mu 2\gamma})$ are efficiencies obtained from Monte-Carlo. $BR(K_{\mu 2\gamma})$ is taken from theory because

an experimental measurement is very old and has a large error (the mean value is consistent with the theoretical prediction). In future, this *BR* could be measured using ISTRA+ data.

$BR(K \to \mu\nu_h)$ is substituted by the following expression:

$$BR(K \to \mu\nu_h) = BR(K_{\mu 2}) \cdot |U_{\mu h}|^2 \cdot f(m_h).$$

Here $BR(K_{\mu 2})$ is taken from PDG [17], $f(m_h)$ contains chirality flip and phase space factors. For Dirac case from the general formula in [18] we get:

$$f_D(m_h) = \frac{m_h^2(1-\frac{m_h^2}{m_K^2}+2\frac{m_\mu^2}{m_K^2}+\frac{m_\mu^2}{m_h^2}(1-\frac{m_\mu^2}{m_K^2}))}{m_\mu^2(1-\frac{m_\mu^2}{m_K^2})^2} \cdot \sqrt{(1+\frac{m_h^2}{m_K^2}-\frac{m_\mu^2}{m_K^2})^2-4\frac{m_h^2}{m_K^2}}.$$

For Majorana case, $f_M(m_h) = 2 \cdot f_D(m_h)$.

Finally for $|U_{\mu h}|^2$ we get

$$|U_{\mu h}|^2 = \frac{N_{exp}(K \to \mu\nu_h)}{N_{exp}(K_{\mu 2\gamma})} \frac{BR(K_{\mu 2\gamma})}{BR(K_{\mu 2})} \frac{\varepsilon(K_{\mu 2\gamma})}{\varepsilon(K \to \mu\nu_h)} \frac{1}{f(m_h)}.$$

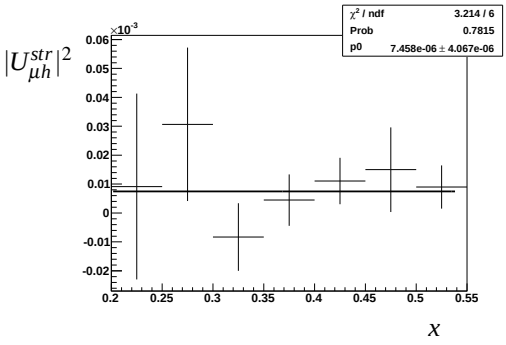

Figure 11: Final fit, m=50MeV, $\tau = 10^{-10} sec.$ Dirac case.

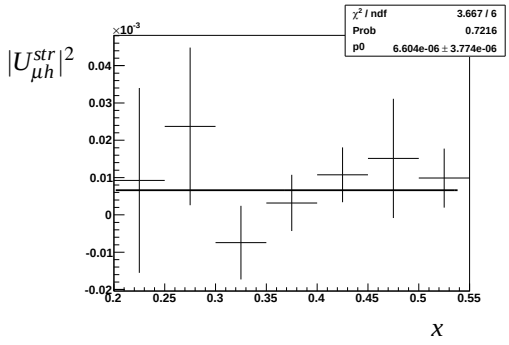

Figure 12: Final fit, m=50MeV, $\tau = 10^{-10} sec.$ Majorana case.

5.2 Averaging $|U_{\mu h}|^2$ and setting upper limits

Values $|U_{\mu h}|^2$ are calculated for all seven *x*-stripes (we will denote them as $|U_{\mu h}^{str}|^2$) and then averaged ($|U_{\mu h}^{av}|^2$). We call this averaging procedure a final fit. The averaged value is used for one-sided upper limit (U.L.) calculation:

$$U.L.(95\%C.L.) = |U_{\mu h}^{av}|^2 + 1.64 \cdot \sigma_{U,tot}.$$

Here $\sigma_{U,tot}$ is a total error of $|U_{\mu h}^{av}|^2$ measurement.

The final fit for a certain (m_h, τ_h) is shown in Fig. 11 (Dirac case) and Fig. 12 (Majorana case). The effect in $|U_{\mu h}^{av}|^2$ (only statistical error is considered here) does not exceed $1 \div 2\sigma$ for all (m_h, τ_h) and hence an upper limit should be set.

5.3 Systematic error

Main sources of systematics are:

- fit systematics;
- cut on x (number of x-stripes in the final fit);
- cut on y in x-stripes;
- x-stripe width;
- bin size in y and $cos\theta_{\mu\gamma}$ histograms.

The largest contribution to the total systematic error comes from the **fit systematics** caused by non-ideal MC shapes of the signal and the backgrounds. To estimate this systematic error the following procedure is used:

- errors for $|U_{\mu h}^{str}|^2$ are scaled for each x-stripe proportionally to $\sqrt{\chi^2/n.d.f.}$;
- averaging is repeated with these new scaled errors;
- new averaged value $|U_{\mu h}^{av,scaled}|^2$ has larger error σ_{scaled} which is treated as $\sigma_{scaled} = \sqrt{\sigma_{stat}^2 + \sigma_{syst,fit}^2}$. Here σ_{stat} is a statistical error of $|U_{\mu h}^{av}|^2$.

Systematics of a **cut on x** is estimated as follows:

- averaging is done for different number of x-stripes in the fit (varying cut on x);
- the dependence of $|U_{\mu h}^{av}|^2$ on x-cut is fitted by a straight line;
- the slope of this line multiplied by the x-stripe width is the estimation of systematic error.

Details of this procedure are described in [13].

Systematics of a **cut on y** is calculated in a similar way by varying y-cut value and fitting the dependence of $|U_{\mu h}^{av}|^2$ on y-cut by a straight line.

x-stripe width is changed ($dx = 0.035, dx = 0.07$) and the whole procedure (simultaneous fits in x-stripes, final fit) is repeated for new dx. New values of $|U_{\mu h}^{av,new}|^2$ are compatible with old ones and hence no systematics is found here.

Systematics caused by the **bin size in y and cos $\theta_{\mu\gamma}$ histograms** is estimated in a similar way and the result is the same: no additional error is found.

5.4 Upper limits

Upper limits for different lifetimes as a function of m_h are shown in Figs. 13 – 18. They could be compared with the region predicted in [6]. As an example, contribution of all errors to the final result is shown in Table 1 for the Dirac case, $\tau = 10^{-10} sec$. Exact numbers are collected in Tables 2 and 3.

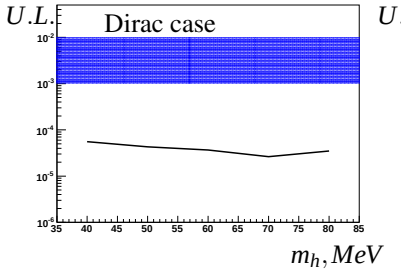

Figure 13: Upper limit for $|U_{\mu h}|^2$ vs m_h for $\tau = 10^{-9} sec$.

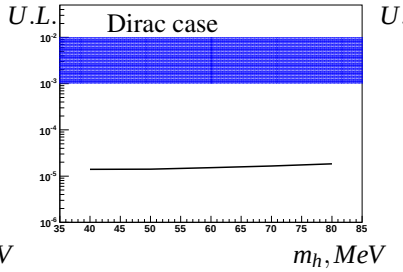

Figure 14: Upper limit for $|U_{\mu h}|^2$ vs m_h for $\tau = 10^{-10} sec$.

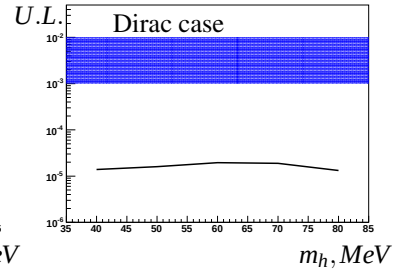

Figure 15: Upper limit for $|U_{\mu h}|^2$ vs m_h for $\tau = 10^{-11} sec$.

In Figs. 13–18 black line corresponds to obtained upper limits, blue stripe – to prediction from [6].

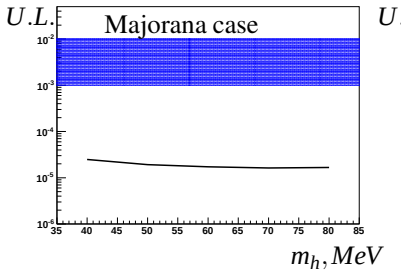

Figure 16: Upper limit for $|U_{\mu h}|^2$ vs m_h for $\tau = 10^{-9} sec$.

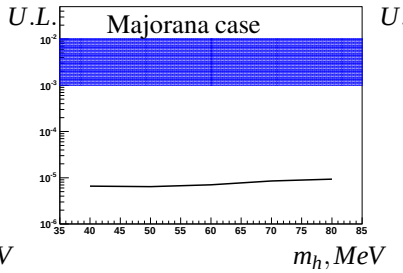

Figure 17: Upper limit for $|U_{\mu h}|^2$ vs m_h for $\tau = 10^{-10} sec$.

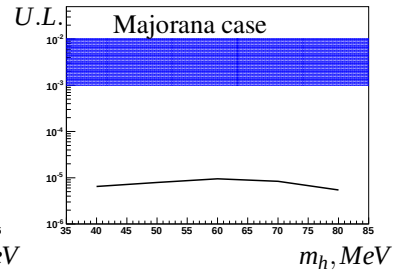

Figure 18: Upper limit for $|U_{\mu h}|^2$ vs m_h for $\tau = 10^{-11} sec$.

m, MeV	$\lvert U_{\mu h}\rvert^2$	σ_{stat}	$\sigma_{syst,x}$	$\sigma_{syst,y}$	$\sigma_{syst,fit}$	$U.L.$
40	0.7	0.4	0.01	0.009	0.5	1.8
50	0.7	0.4	0.02	0.004	0.5	1.8
60	0.8	0.4	0.01	0.03	0.5	1.9
70	0.9	0.5	0.005	0.2	0.5	2.0
80	1.0	0.5	0.01	0.3	0.6	2.3

Table 1: Dirac type, $\tau = 10^{-10} sec$. Fit results and $U.L.$'s are in 10^{-5} units.

m, MeV	$U.L., \tau = 10^{-9} sec$	$U.L., \tau = 10^{-10} sec$	$U.L., \tau = 10^{-11} sec$
40	7.0	1.8	1.8
50	5.4	1.8	2.0
60	4.6	1.9	2.4
70	3.4	2.1	2.5
80	4.2	2.4	1.9

Table 2: Dirac type. $U.L.$'s are in 10^{-5} units.

m, MeV	$U.L., \tau = 10^{-9} sec$	$U.L., \tau = 10^{-10} sec$	$U.L., \tau = 10^{-11} sec$
40	3.3	0.9	0.9
50	2.6	1.0	1.0
60	2.2	1.0	1.4
70	2.2	1.3	1.2
80	2.2	1.6	1.0

Table 3: Majorana type. $U.L.$'s are in 10^{-5} units.

6. Conclusions

We have performed a search for a heavy neutrino of Dirac and Majorana type in $K \to \mu\nu_h(\nu_h \to \nu\gamma)$ decay assuming that ν_h is a part of ν_μ flavor eigenstate and decays radiatively into a massless neutrino and a photon and obtained upper limits at 95% C.L. for the mixing matrix element $|U_{\mu h}|^2$.

The upper limit at 95% C.L. in a mass region $40MeV \leq m_h \leq 80MeV$ for $10^{-11}sec \leq \tau \leq 10^{-9}sec$ is $U.L. \sim (1 \div 3) \cdot 10^{-5}$ (Majorana type of ν_h) and $U.L. \sim (2 \div 7) \cdot 10^{-5}$ (Dirac type). The obtained values close the allowed region for $|U_{\mu h}|^2$ suitable for LSND/KARMEN/MiniBooNE anomaly explanation proposed in [6].

Authors would like to thank S.N.Gninenko, D.S.Gorbunov, V.A.Rubakov, A.A.Saratov (INR RAS) and R.Shrock (YITP, Stony Brook) for numerous discussions. The work is supported by Russian Fund for Basic Research (grants 10-02-00330-a and 11-02-00870-a).

References

[1] A.Aguilar et al.,Phys.Rev. D64, 112007 (2001).

[2] A.A.Aguilar-Arevalo et al., Phys. Rev. Lett. 102, 101802 (2009).

[3] A.A.Aguilar-Arevalo et al., arXiv: 1007.1150 [hep-ex].

[4] B.Armbruster et al., Phys. Rev. D 65, 112001 (2002).

[5] J.Kopp, M.Maltoni, T.Schwetz, arXiv:1103.4570.

[6] S.N.Gninenko, Phys. Rev. D 83, 015015 (2011).

[7] S.N.Gninenko, Phys. Rev. Lett. 103, 241802 (2009).

[8] R.Shrock, Phys.Rev. D9, 743 (1974); B.W.Lee and R.Shrock, Phys.Rev. D16, 1444(1977).

[9] Phys.Lett. 96B, 159 (1980); Phys.Rev. D24, 1232 (1981), Phys.Rev. D24, 1275 (1981).

[10] R.Abela et al., Phys. Lett. B 105, 263 (1981).

[11] R.S.Hayano et al., Phys. Rev. Lett. 49, 1305 (1982).

[12] V.N.Bolotov et al. IHEP preprint 8-98,1998.

[13] V.A.Duk et al., Phys. Lett. B 695: 59-66 (2011).

[14] I.V.Ajinenko et al. Phys.Atom.Nucl. 66(2003) 105; Yad.Fiz. 66 (2003) 107.

[15] O.P.Yushchenko et al. Phys.Lett. B581 (2004) 31.

[16] F. James, M. Roos. CERN-DD-75-20, Jul 1975.

[17] K.Nakamura et al. (Particle Data Group), J. Phys. G 37, 075021 (2010).

[18] D.Gorbunov and M.Shaposhnikov, JHEP 0710, 015 (2007).